Flow separation and rotor formation beneath two-dimensional trapped lee waves

By S. B. VOSPER*, P. F. SHERIDAN and A. R. BROWN
Met Office, UK

SUMMARY

Numerical simulations of trapped lee waves generated in flow over a two-dimensional ridge are presented. It is shown that for sufficiently large amplitude waves flow separation occurs beneath the wave crests when a no-slip lower boundary condition is applied. The occurrence of separation corresponds to rotor motion, or recirculation, under the wave crests. The dependence of the wave-induced horizontal flow perturbations near the ground on the wave amplitude, wavelength and surface roughness is examined. It is shown that the normalized critical wave amplitude, above which rotors form, is a function of the ratio of the lee-wave horizontal wavelength to the surface roughness length. This normalized wave amplitude is defined as the ratio of the lee-wave pressure amplitude within the boundary layer, to the square of the friction velocity.

Linearized turbulent equations for motion beneath the wave crests are considered and numerical solutions to the linear problem are compared with results from the simulations. When the waves are of sufficiently small amplitude that flow separation does not occur, the linear flow perturbations are shown to agree closely with the results from the simulations. It is also shown that linear theory provides a useful prediction of the occurrence of rotor formation.

KEYWORDS: Boundary layer   Linear theory   Orography

1. INTRODUCTION

It is well known that mountain waves are sometimes associated with damaging winds and severe turbulence, both near the ground and aloft. Such effects pose a threat to aviation safety, particularly during take-off or landing manoeuvres, as well as causing damage on the ground. Hertenstein and Kuettner (2005), in a recent numerical study, categorized mountain-wave induced turbulence into two kinds: type 1 and type 2 rotors. Type 1 are the regions of turbulent recirculating airflow which occur under the crests of a laminar trapped lee-wave train, whereas type 2 are associated with low-level gravity-wave breaking, whose structure is similar to that of a hydraulic jump (Baines 1995). In this study we shall focus on type 1, or lee-wave rotors.

Currently little is known about the structure of lee-wave rotors, or the conditions under which they occur. In comparison, as recently pointed out by Hertenstein and Kuettner (2005), mountain waves themselves have received considerable attention over the last few decades. The impact of the waves on the near-surface flow and the processes which lead to the formation of rotors, have not. Notable exceptions to this include a small number of observational studies, which date as far back as the pioneering measurements made above the Alps and the Sierra Nevada (e.g. Kuettner 1939; Holmboe and Klieforth 1957). More recently, observational studies include those made by Ralph *et al.* (1997) and Mobbs *et al.* (2005). Recently Doyle and Durran (2002) examined the dynamics of lee-wave rotors with a series of numerical simulations. Their study highlighted the importance of surface friction in allowing rotors to form. When the wave response is of sufficient amplitude, the wave-induced pressure gradient can lead to boundary-layer separation and regions of recirculation underneath the wave crests. This effect was also noted by Vosper (2004) in numerical simulations of rotors under the crests of lee-waves which formed on a sharp temperature inversion. Note that this concept is not new, and in fact a very early study by Lyra (1943) noted that the lee-wave pressure gradient may

* Corresponding address: Met Office, FitzRoy Road, Exeter EX1 3PB, UK.
e-mail: simon.vosper@metoffice.gov.uk

drive rotor recirculations. Importantly, however, Lyra's model did not take any account of boundary-layer processes.

Compared to lee-wave induced flow separation over flat ground, for two-dimensional (2-D) orography at least, separation in neutrally stratified turbulent flow over hills is reasonably well understood. In this case the flow is essentially controlled by a perturbation pressure field which is determined by inviscid dynamics in the outer region of the flow. This inviscid outer region lies above the inner region, where the hill-induced turbulent stresses play an important dynamical rôle. Negative pressure perturbations above the summit and positive values over the lee slope lead to deceleration downwind of the crest, which generates horizontal vorticity of the opposite sign to the boundary-layer vorticity. For sufficiently large slopes the pressure field induces vorticity which overcomes the boundary-layer vorticity, leading to flow separation and reversed flow. The study by Wood (1995) highlighted the importance of the hill horizontal length-scale (or wavelength) and the surface roughness in determining whether the flow over a hill with a given slope will separate. Both these factors affect the magnitude of the velocity-scale near the ground, an increase in which requires a corresponding increase in the outer-region pressure gradient to reverse the flow. The flow is less prone to separation over smooth or long hills. This latter dependence is due to the tendency for the inner-region depth to grow with increasing wavelength, leading to an increase in the inner-region velocity-scale.

Although there are clearly fundamental differences between the processes of flow separation over hills and lee-wave rotor formation, the two phenomena do share one common feature. Both are controlled to a large degree by the size of a pressure gradient which is imposed on the near-surface flow. In the hill case this pressure gradient is, to a good approximation, determined by the outer-region inviscid dynamics and is unaffected by the turbulent processes within the inner region. Similarly Doyle and Durran (2002) demonstrated a possible relationship between lee-wave rotor strength (as measured by the strength of reversed flow) in no-slip simulations and the pressure gradient which occurred in otherwise identical free-slip simulations. These similarities hint that we might expect lee-wave rotors to depend on the surface roughness and wavelength in an analogous way. In the lee-wave case, however, the relevant wavelength would presumably be that of the waves rather than the orography.

As discussed by Wood (1995), in reality a fully turbulent flow may contain intermittent separation due to the presence of intense turbulent eddies. However, numerical study of such intermittent separation would require three-dimensional (3-D) eddy-resolving modelling which is beyond the scope of this paper. Here we shall restrict our attention to the process of mean flow separation. The main aim of this paper is to study the mechanisms by which trapped lee waves affect the near-surface flow and, ultimately, to predict the critical lee-wave amplitude required for the onset of flow separation, which leads to the formation of rotors. Following on from the study by Doyle and Durran (2002), we shall concentrate primarily on the relationship between the lee-wave pressure field and the strength of the flow perturbations near the ground.

The remainder of the paper is set out as follows. The numerical model used in this study is described in section 2 and a series of 2-D numerical simulations of lee waves is described in section 3. The results are used to study the relationship between the lee-wave pressure amplitude and the strength of the recirculating flow beneath the wave crests. Simulations of flows with a range of surface roughness lengths and lee-wave wavelengths are then used to produce an empirical prediction of the critical wave amplitude required for rotor formation. In section 4 a set of linearized equations of motion are presented for the turbulent flow beneath the wave crests. Numerical solutions

to these equations are obtained and it is shown that, in general, the linear prediction for the deceleration beneath the wave crests agrees well with the earlier results of the 2-D numerical simulations, up to the point where the waves are of sufficient amplitude that rotors form. The analogy between the lee-wave flow and turbulent flow over a hill is also examined by comparing the results with linear theory for the latter. Conclusions are drawn in section 5.

2. THE NUMERICAL SIMULATIONS

(a) Model description

The numerical model employed for this study was the Met Office BLASIUS model (Wood and Mason 1993). This has been used extensively for studies of both neutral and stably stratified flows over hills and mountains (e.g. Wood 1995; Ross and Vosper 2003; Vosper 2004). The model is based on the time-dependent Boussinesq or anelastic equations for a terrain-following coordinate system (Gal-Chen and Somerville 1975). The equations are discretized using finite differences; a second-order accurate scheme is used for advection of velocity (Piacsek and Williams 1970) and the Leonard *et al.* (1993) Ultimate-Quickest scheme is used for advection of potential temperature. The present study is based on the Boussinesq equations and a first-order Richardson number-dependent mixing-length turbulence closure scheme. The maximum mixing length used in all simulations was 40 m.

The model domain consisted of 1024 grid points in the x (streamwise) direction and 60 levels in the vertical. The lowest grid point above the ground was at 10 m and the vertical grid was stretched such that the grid spacing increased smoothly with height from 20 to 614 m adjacent to the upper boundary, which was placed at 20 km. The horizontal resolution in all simulations was 200 m. The upper boundary condition was a rigid lid and a Rayleigh damping layer was placed above 15 km in order to minimize the reflection of upward-propagating gravity waves. The damping coefficient in this layer increased smoothly from zero, at the bottom of the layer, to a maximum value at the upper boundary. The model lateral boundary conditions were periodic and following Vosper (2004) damping columns were applied at both the upwind and downwind boundaries in order to avoid wrap-around effects. These were 8 km wide and, as for the upper layer, the damping coefficient in these columns increased smoothly towards the boundaries.

(b) Configuration of the simulations

The ridge considered in this study had the commonly used Witch of Agnesi form, specified by

$$h(x) = H/(1 + x^2/L^2), \qquad (1)$$

where H and L are the mountain height and half-width, respectively. The value of L was chosen to be 2 km and simulations were conducted for a range of heights. Most of the results presented here are for lee waves generated in an idealized flow whose basic state consisted of a sinusoidal westerly jet described by

$$\overline{U}(z) = U_0 + U_t \sin(\pi z/z_{\mathrm{m}}), \qquad (2)$$

where U_0 is the surface wind speed and $z_{\mathrm{m}} = 20$ km is the depth of the model domain. The value of U_0 chosen was 5 m s^{-1} and two different values of U_t were considered: 28 and 36 m s^{-1}, giving maximum jet strengths of 33 and 41 m s^{-1}, respectively.
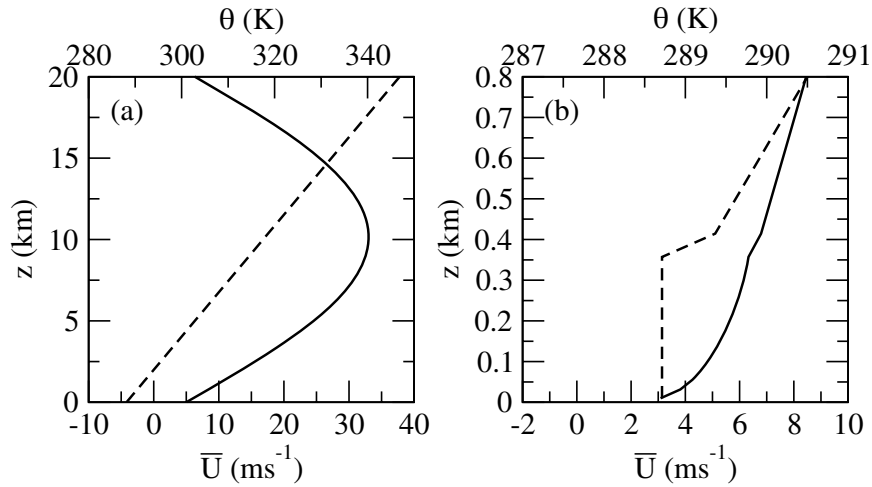
Figure 1.   The idealized profiles of wind $\overline{U}$ (solid line) and potential temperature (dashed) used in the simulations ($U_0 = 5$ m s^{-1}, $U_t = 28$ m s^{-1}) both (a) before and (b) after modification by boundary-layer mixing with a roughness length of 0.05 m. These profiles were used to initialize the 2-D BL and FS simulations, respectively (see text). Note only the lowest portion of the profile is shown in (b) as above the boundary layer the profile is identical to that shown in (a).

The basic-state potential temperature increased linearly with height, yielding a constant Brunt–Väisälä frequency N which was equal to 0.01 s^{-1}. Examples of the above wind and potential-temperature profiles are shown in Fig. 1(a). Additional simulations have been conducted using data from real radiosonde ascents launched from Hazelrigg weather station near Lancaster (2.7°W, 54.1°N) in north-west England. These radiosondes were launched as part of a programme of field measurements aimed at studying lee waves and associated rotors downwind of the Pennines in northern England. The results from this study are not presented here, but two of the radiosonde profiles obtained when lee waves were observed across the Pennines will be used to initialize the simulations across the 2-D idealized ridge. These ascents were made on 17 March and 6 December 2004. For both ascents the velocity data were resolved along a south-westerly direction, which was approximately the wind direction at the top of the boundary layer. The velocity and potential-temperature profiles are presented in Fig. 2.

The extent to which gravity waves are trapped is largely determined by the well-known Scorer parameter, $\ell^2(z)$ (Scorer 1949), which appears in the linear vertical structure equation,

$$\frac{\mathrm{d}^2\widehat{w}}{\mathrm{d}z^2} + (\ell^2 - k^2)\widehat{w} = 0, \qquad (3)$$

where $\widehat{w}(k, z)$ is the Fourier transformed vertical velocity and k is the horizontal wave number. The precise form of ℓ^2 depends on which approximate equations of motion are considered (see Nance 1997). For the shallow-convection form of the Boussinesq equations in which density is considered independent of height, ℓ^2 is given by

$$\ell^2(z) = \frac{N^2}{\overline{U}^2} - \frac{1}{\overline{U}}\frac{\mathrm{d}^2\overline{U}}{\mathrm{d}z^2}. \qquad (4)$$

Profiles of ℓ^2 computed for the idealized and radiosonde profiles are shown in Fig. 3. Note that substantial smoothing was applied to N^2 and $\mathrm{d}^2\overline{U}/\mathrm{d}z^2$ for the radiosonde
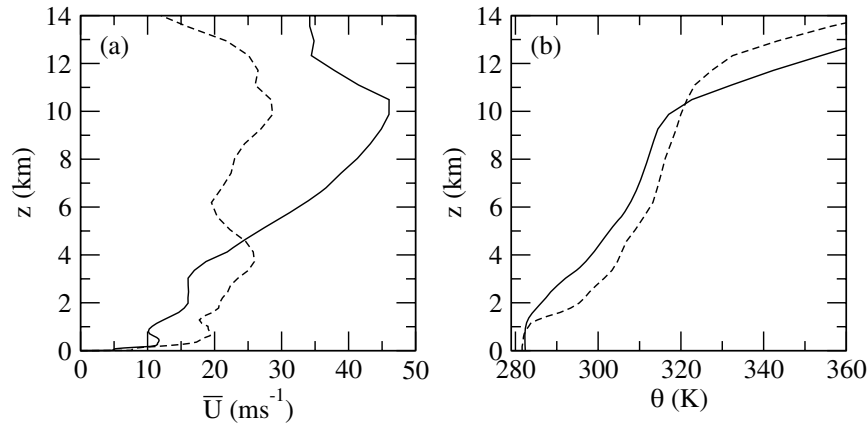
Figure 2. The profiles of (a) wind speed and (b) potential temperature, obtained from the Hazelrigg radiosonde ascents launched at 11 UTC 17 March (solid line) and 09 UTC 6 December 2004 (dashed). The wind data shown are the component of the wind resolved along a direction of 225°.
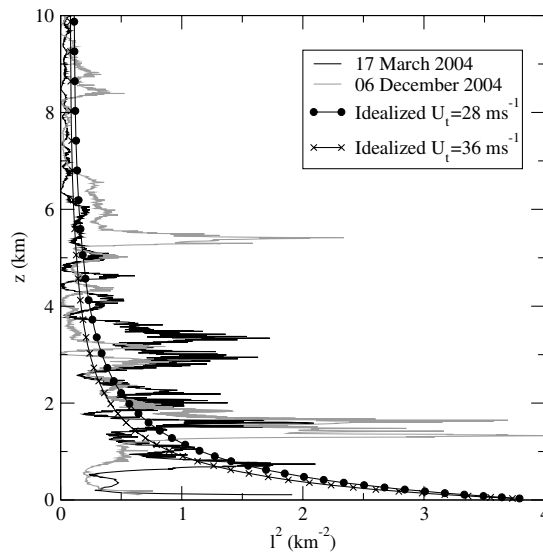
Figure 3. Profiles of the Scorer parameter ℓ^2 (see text) over the lowest 10 km for the idealized profiles with $U_t = 28 \text{ m s}^{-1}$ and $U_t = 36 \text{ m s}^{-1}$ and for profiles obtained from two radiosonde ascents launched from Hazelrigg at 11 UTC 17 March and 09 UTC 6 December 2004.

profile calculation. The general tendency for ℓ^2 to decrease with height through the lower troposphere for all cases indicates that the profiles are conducive to wave trapping.

Three types of simulation have been conducted. In the majority of cases a no-slip lower boundary condition was applied, via a similarity condition for the surface stress, and a range of different (constant) roughness lengths z_0 were considered. In the interests of reducing model integration times a one-dimensional (1-D) boundary-layer solution was first obtained using a 1-D version of the model which was run to a steady state. This resulted in some modification to the wind and potential-temperature profiles within the boundary layer, in which the stratification became neutral. An example of this for the idealized profile with $U_t = 28 \text{ m s}^{-1}$ is shown in Fig. 1(b). The no-slip 2-D simulations

TABLE 1.   THE IDENTIFIERS USED TO DISTINGUISH THE DIFFERENT TYPES OF 2-D SIMULATION

	BL	BLI	FS
Initial 1-D solution calculated?	Yes, with a no-slip lower boundary condition	Yes, with a no-slip lower boundary condition	No solution required
2-D lower boundary condition	No-slip	Free-slip	Free-slip
Turbulence closure applied?	Yes	No	No

were then initialized with these modified 1-D profiles. Throughout the paper these will be referred to as BL simulations. In a second type of simulation a free-slip lower boundary condition was applied (Durran and Klemp 1983). These simulations allowed assessment of the impact of surface friction and the presence of a developed upstream boundary layer. In this case no initial 1-D solution was required. These simulations will be identified by FS. The third kind of simulation was designed to distinguish between the impact on the lee waves of changes to the basic-state profile caused by the boundary layer and the direct effect of turbulent dissipation. For these simulations a 1-D solution was first obtained (using a no-slip boundary condition and turbulence closure scheme) so that the initial profile contained the boundary-layer wind shear and neutral potential-temperature profile. However, the 2-D simulations were inviscid (no turbulence closure was applied) and the free-slip boundary condition was imposed. These simulations will be referred to by the identifier BLI. Note that the lack of viscosity (other than numerical) in these simulations meant that they were only possible for small mountain heights. For values of H greater than around 200 m the solutions contained a high degree of grid-scale noise. The meanings of the three identifiers BL, FS and BLI are summarized in Table 1.

In all cases a zero surface heat-flux condition was applied. The Coriolis force was imposed with $f = 10^{-4}$ s^{-1} and in the no-slip cases this resulted in turning of the boundary-layer wind profile which was absent in the free-slip simulations. Note, however, that for flow over a 2-D ridge the component of the flow parallel to the ridge plays no rôle in the lee-wave dynamics. Model integrations were carried out for 3×10^4 s, by which time steady solutions were obtained.

3.   NUMERICAL RESULTS

Figure 4(a) shows the potential temperature and horizontal velocity component for a 600 m high mountain in the BL simulation with $U_t = 28$ m s^{-1} and $z_0 = 0.05$ m. A large amplitude trapped lee-wave field extends downwind of the mountain with a horizontal wavelength of approximately 10.4 km. Close examination reveals that the waves are of sufficient amplitude to reverse the flow near the ground. This is confirmed by a close-up view of the flow beneath the first two wave crests downwind of the mountain, as shown in Fig. 4(b). This flow reversal is associated with flow separation and rotor motion under the wave crests. In general the flow in free-slip simulations (not shown) does not contain rotors such as these. This is consistent with previous findings (Doyle and Durran 2002; Vosper 2004) which showed that surface friction plays a crucial rôle in allowing rotors to form. Note, however, that in the free-slip simulation equivalent to that presented in Fig. 4, reversal does occur. The recirculation is very weak, however, and reversal does not occur for smaller mountains. In contrast, rotors are present for mountains as low as 290 m in the $U_t = 28$ m s^{-1} BL case. Doyle and Durran (2002) obtained a similar result for a free-slip simulation with a sufficiently high mountain. In their case the wave
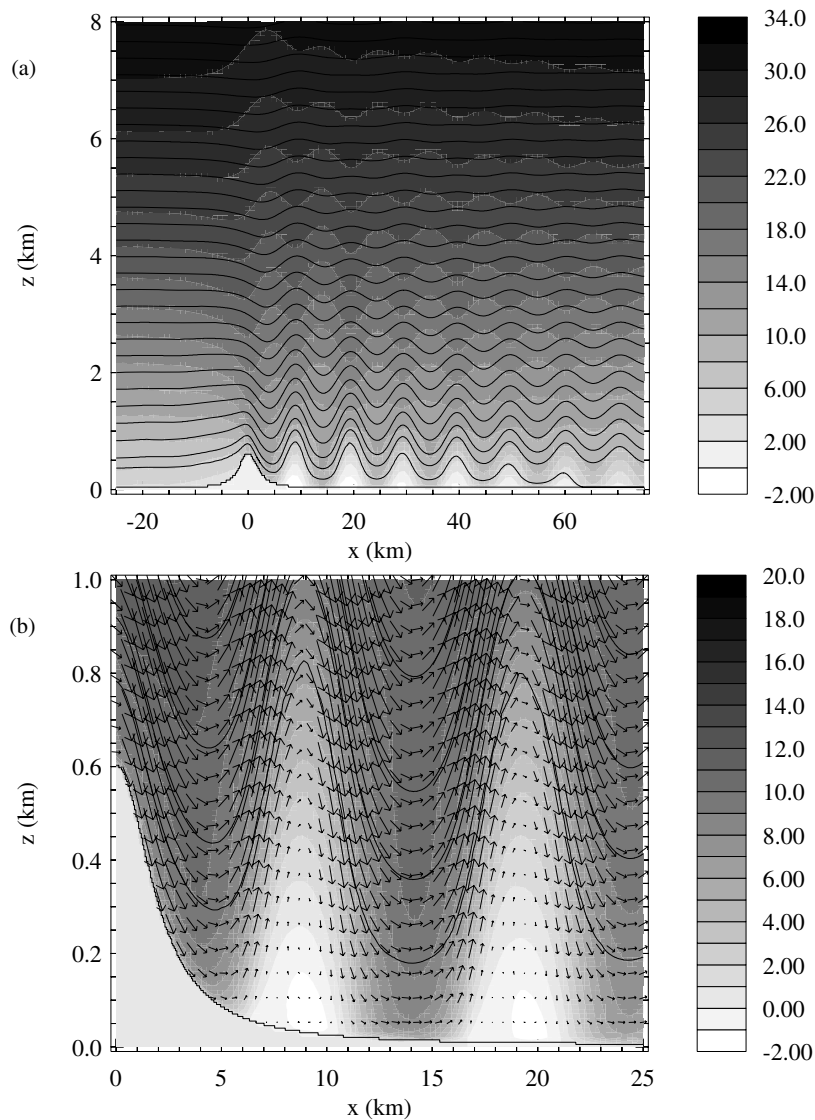
Figure 4. (a) The simulated flow field after 3×10^4 s of integration time for a 600 m high mountain in the $U_t = 28$ m s^{-1}, $z_0 = 0.05$ m BL case. Quantities shown are the horizontal velocity component (shaded contours; units m s^{-1}) and contours of potential temperature (solid contours; interval 1 K). (b) A close-up view, including flow vectors.

amplitude required to reverse the flow was so large that the waves were highly nonlinear and nonstationary.

The results for BL simulations with $U_t = 36$ m s^{-1}, $z_0 = 0.05$ m contain similar lee-wave trains and rotors to those seen in Fig. 4. Consistent with the smaller values of ℓ^2 (see Fig. 3) in this case, the horizontal wavelengths are somewhat longer than for $U_t = 28$ m s^{-1}, at around 14.6 km. The BL simulations based on the radiosonde profiles also contain lee waves and, for sufficiently high mountains, lee-wave rotors. The horizontal wavelengths in this case are similar at around 9.9 and 10.1 km for the 17 March and 6 December 2004 profiles, respectively.
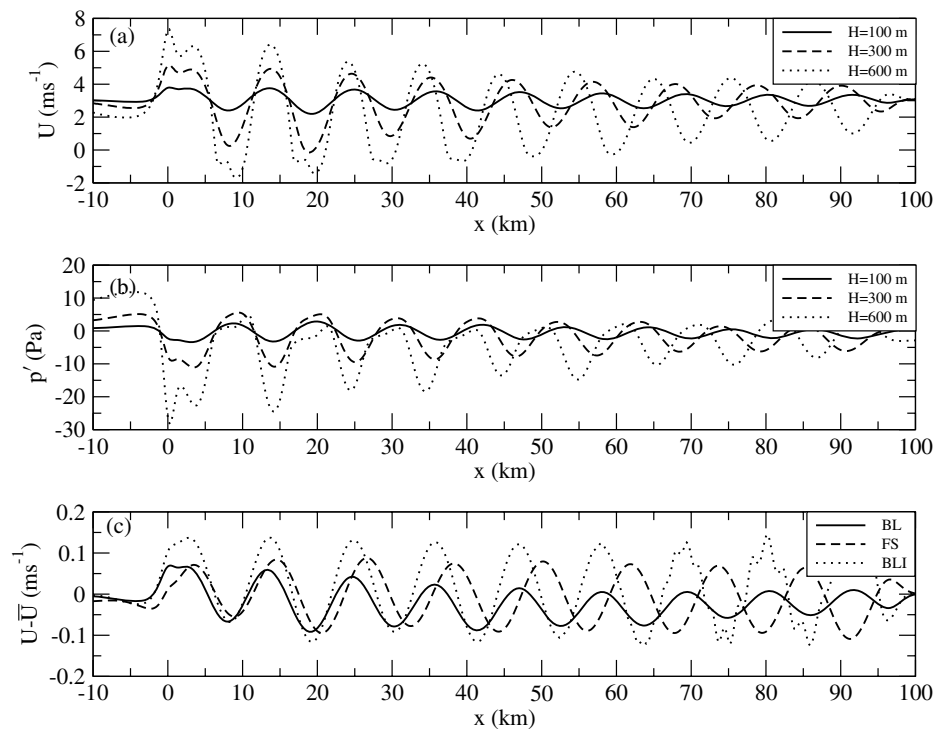
Figure 5.   The horizontal winds on the lowest model level (10 m) and surface pressure for $U_t = 28$ m s^{-1} simulations. (a) Horizontal winds and (b) surface pressure, for BL simulations with mountain heights H of 100, 300 and 600 m and a roughness length of 0.05 m. (c) The horizontal wind component after removal of the basic-state value for $H = 10$ m BL, FS and BLI simulations (see text).

One measure of the strength of the rotors is the strength of the reversed flow. Figure 5(a) shows the horizontal variation of the horizontal wind component on the lowest grid level (10 m) in the $U_t = 28$ m s^{-1}, $z_0 = 0.05$ m BL simulations for three mountain heights, namely 100, 300 and 600 m. The amplitude of the wind-speed fluctuations clearly increases with increasing mountain height and reversal occurs for the two higher mountain cases. It is interesting to note that the horizontal wavelength exhibits some slight decrease with increasing hill height. When $H = 100$ m, for example, the horizontal wavelength deduced from Fig. 5 is approximately 11.2 km and this is reduced to roughly 10.4 km when $H = 600$ m. It seems likely that this behaviour is due to the increased importance of nonlinearity as the mountain height increases, which presumably results in subtle modifications to the mean flow, thus altering the resonant lee-wave response. Figure 5(a) also reveals a tendency for the wave amplitude to decrease with downstream distance. Whilst it is possible that this apparent damping of the wave motion is due to numerical dissipation, this is unlikely given that results from tests in which the horizontal grid scale was reduced by a factor of 2 (not shown) were nearly identical to those shown here. Figure 5(c) shows the 10 m wind, after removal of the basic-state value, for three simulations with a very small mountain of height 10 m. The results for the BL simulation show a gradual decrease of wave amplitude away from the mountain, consistent with that observed for the higher mountain cases shown in Fig. 5(a). It seems unlikely, therefore, that nonlinearity alone can explain the amplitude decrease. The results from an equivalent FS simulation, however, do not show any signs

of amplitude decay, indicating that perhaps boundary-layer processes are responsible. The results from a further inviscid BLI simulation, in which the basic-state profile contains the same wind and potential-temperature boundary-layer structure as the BL case, also show no signs of amplitude decay. It would appear, therefore, that the damping is due to the direct effect of the boundary-layer dissipation on the wave motion, rather than changes to the upwind profile such as boundary-layer shear or neutral stratification. This downstream decay of wave amplitude is consistent with the recent theoretical ideas put forward by Smith *et al.* (2006), which are supported by numerical simulations (Jiang *et al.* 2006). In Smith's shallow-layer representation the boundary layer acts to partially absorb energy associated with the downward-propagating part of trapped wave motion, thus progressively reducing the amplitude downstream. This amplitude reduction is seemingly connected with the upwind phase shift of the boundary-layer wind response (see Fig. 5(c) and discussion later) and the associated flow divergence which changes the boundary-layer thickness. The differences in phase between the lee-wave vertical motion aloft and the vertical motion within the boundary layer act to absorb downward-propagating wave motion and advance the phase of reflected waves.

Figure 5(b) shows the horizontal variation of the surface pressure perturbation p' for the $U_t = 28$ m s^{-1} BL cases which correspond to the surface winds shown in Fig. 5(a). The surface pressure fluctuations also exhibit a tendency to decrease with increasing downwind distance. Comparison of Figs. 5(a) and (b) shows that the horizontal velocity and pressure perturbation signals are not exactly 180° out of phase. Indeed, the minima in U are located slightly upwind of the pressure maxima. Although not shown here, the surface pressure results for the FS and BLI cases of Fig. 5(c) do not exhibit this behaviour. It seems likely, therefore, that the upwind phase shift of the velocity (relative to the surface pressure fluctuations) in the turbulent no-slip flows are due to the influence of the turbulent stresses. Note that a similar effect is known to occur in neutral turbulent flow across a hill (e.g. Newley 1985) where the maximum wind speeds near the surface occur just upwind of the hill crest. In this case the upwind phase shift is due to the perturbation turbulent shear stress gradient which has a decelerating effect on the flow, opposing the acceleration towards the hill summit by the pressure gradient. Similar phase shifts are also noted by Smith *et al.* (2006) who provided a simple explanation of this behaviour by representing the boundary layer as a thin Rayleigh friction layer. Considering the linearized horizontal momentum equation, the friction causes an upwind phase shift of the horizontal velocity perturbation within the boundary layer. In the limit of large friction the location of the maximum flow speed would coincide with that of the maximum (negative) pressure gradient, rather than the perturbation pressure.

We shall now examine the flow below an individual wave crest and focus attention on the second lee-wave crest downwind of the mountain. Since we are concerned with the influence of the trapped waves, the second wave crest was chosen in preference to the first, as the latter is more likely to be influenced by vertically propagating waves local to the mountain. Figure 6(a) shows the dependence on H of the minimum horizontal velocity component U_{min} under the second lee-wave wave crest for FS and BL simulations with $U_t = 36$ and 28 m s^{-1}. The data shown are for the lowest grid level. In the BL cases results for two values of roughness length are presented, namely 0.05 and 0.005 m. As expected there is a clear tendency for U_{min} to decrease monotonically with increasing H. In the case of the free-slip simulations this decrease is approximately linear for mountain heights less than around 350 m and for greater heights the rate of decrease is somewhat reduced. Given that the non-dimensional mountain height, NH/U_0, is 0.7 when $H = 350$ m, it seems likely this change in behaviour is due to
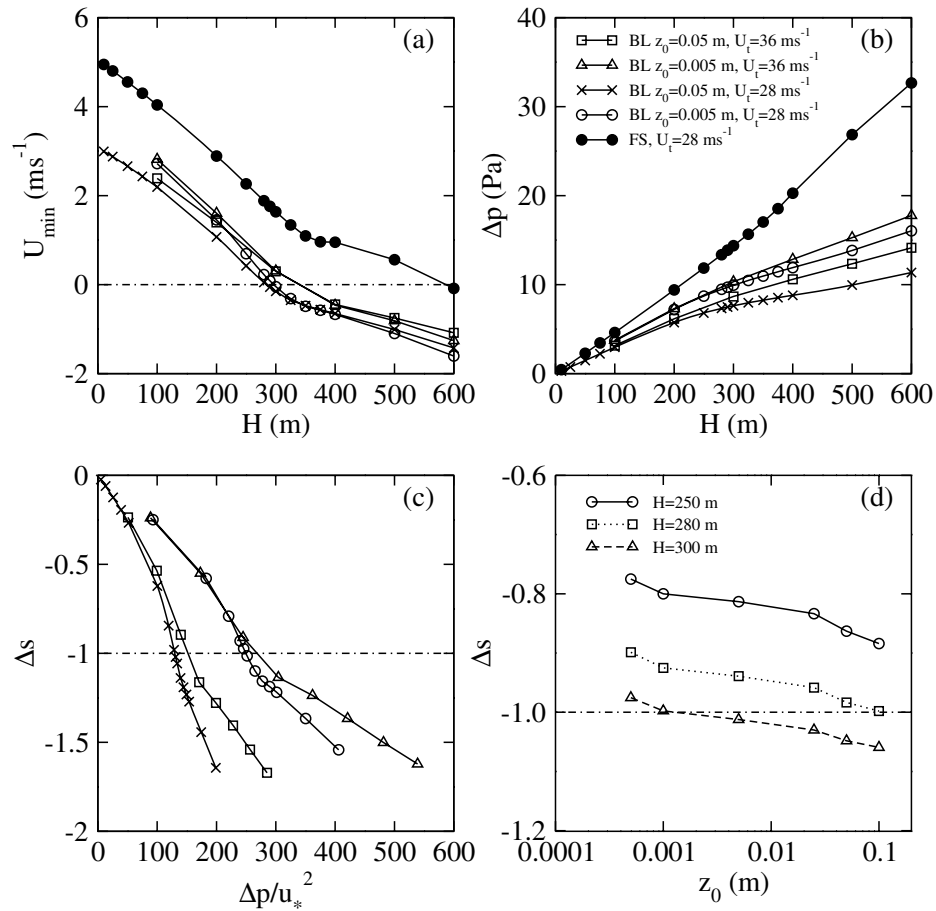
Figure 6. The variation of (a) the minimum horizontal component of velocity, U_{min} at the lowest grid level, and (b) the pressure amplitude Δp with mountain height under the second lee-wave crests for BL simulations with $U_t = 28$ m s^{-1} and 36 m s^{-1} and for FS simulations with $U_t = 28$ m s^{-1}. Results for the BL simulations are shown for roughness lengths of 0.05 and 0.005 m. (c) The fractional deceleration Δs on the lowest grid level as a function of $\Delta p/u_*^2$, where u_* is the basic-state friction velocity. (d) The dependence of Δs on roughness length is shown for fixed mountain heights of 250, 280 and 300 m in the $U_t = 28$ m s^{-1} BL case.

the increasing nonlinear nature of the flow. Flow reversal (and hence rotor formation) occurs in the no-slip cases for mountain heights around 300 m, though the precise value at which reversal first occurs clearly depends on the value of z_0 and U_t, with rotors forming for slightly lower mountains with the higher roughness length and lower wind speeds.

The surface values of the pressure amplitude Δp are shown in Fig. 6(b). Here Δp is defined as half the peak-to-trough pressure perturbation amplitude across the second wavelength. This was estimated by measuring half the average difference between the second maxima in p' downwind of the summit and the two minima located immediately up and downwind. Figure 6(b) shows that Δp increases monotonically with H in all cases. The values for the free-slip simulations are consistently larger than those in the equivalent no-slip simulations. Further, for fixed values of U_t the size of Δp in the BL cases clearly increases with decreasing z_0.

One non-dimensional measure of the rotor strength is the fractional deceleration Δs defined as

$$\Delta s(z) = \frac{U_{\min} - U_\lambda}{U_\lambda}, \tag{5}$$

where $U_\lambda(z)$ is the mean horizontal velocity component at height z measured across a lee-wave wavelength. Values of Δs below -1 correspond to situations of reversed flow. Where $\Delta s \leq -1$ on the lowest model grid level, flow separation occurs and rotors form beneath the wave crests. Note that in Eq. (5) normalization by U_λ is preferred to the basic state $\overline{U}$ because of the possibility of alteration to the mean flow by longer (untrapped) waves, or by momentum transfer via turbulent or wave drag. In practise, however, the results are not sensitive to this choice up until the point where rotors form under the wave crests. In this situation there is clearly some modification to the mean flow. Figure 6(c) shows Δs (on the lowest grid level) beneath the second wave crest in the BL cases. The data are plotted against the normalized pressure amplitude, $\Delta p/u_*^2$, where u_* is the basic-state friction velocity, determined from the 1-D solutions. The fractional deceleration is clearly correlated with $\Delta p/u_*^2$, although the variation depends on the values of z_0 and U_t. Interestingly the curves for different values of U_t, but the same roughness lengths, show signs of collapse where $\Delta s > -1$. As we shall see later, this collapse is connected with the ratio of the lee-wave horizontal wavelength to the roughness length.

As with turbulent flow over a hill (Wood 1995), it would seem that the occurrence of separation beneath lee-wave crests depends to some extent on the surface roughness. This is demonstrated by Fig. 6(d) which shows the variation of Δs (on the lowest grid level) with z_0 for series of $U_t = 28$ m s^{-1} BL simulations with fixed mountain heights of 250, 280 and 300 m. In all cases the fractional deceleration becomes stronger (Δs becomes increasingly negative) as the roughness length increases. For the $H = 300$ m case, increasing the roughness length from 5×10^{-4} m to 0.05 m results in rotor formation.

The critical normalized pressure amplitude, $\Delta p/u_*^2$, at which rotors first form under the second wave crest is shown in Fig. 7 as a function of λ/z_0, where λ is the lee-wave horizontal wavelength. These critical amplitudes were deduced by linear interpolation between simulations with different mountain heights in which rotors did and did not occur. The results from six series of BL simulations with two different values of U_t (28 and 36 m s^{-1}) and three different roughness lengths (0.005, 0.01 and 0.05 m) are shown in Fig. 7. The data show signs of collapse onto a single curve when presented in this manner, implying that the normalized critical wave amplitude is a function of λ/z_0. This idea is also supported by results from linear theory discussed in section 4. Note that alternative normalizations of the pressure amplitude (e.g. by $\overline{U}^2$ evaluated at the inner-layer height or boundary-layer top) do not collapse onto a single curve. Values of the critical $\Delta p/u_*^2$ for the two radiosonde simulations and the same three values of z_0 are also shown in Fig. 7. These appear to behave in a similar way, although interestingly they do not collapse onto the same curve as the idealized simulations. The precise reason for this is not clear and we shall return to this point in section 4.

Note that the result implied by Fig. 7 is analogous to the occurrence of flow separation in neutrally stratified turbulent flow over a hill. As shown by Wood (1995), according to linear theory the critical hill slope at which separation first occurs is an increasing function of the ratio of hill wavelength to roughness length. The analogy becomes clearer when one considers that in neutral flow over a hill, the pressure amplitude scales with the hill slope times the square of a velocity-scale.
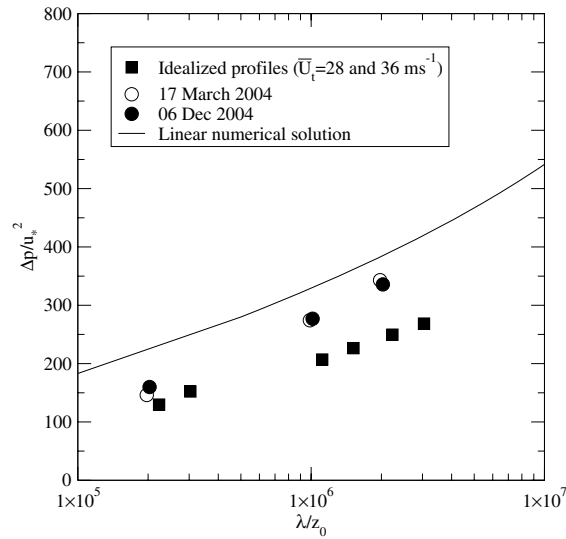
Figure 7. The critical normalized pressure amplitude, $\Delta p/u_*^2$, at which flow separation first occurs under the second wave crest. The squares denote results from six series of BL simulations with two different values of U_t (28 and 36 m s^{-1}) and three different roughness lengths (0.005, 0.01 and 0.05 m). The data are plotted as a function of λ/z_0, where λ is the lee-wave horizontal wavelength. Also shown are the results for simulations with the 17 March (open circles) and 6 December 2004 (filled circles) radiosonde profiles with the same three values of z_0. The linear theory prediction of the critical $\Delta p/u_*^2$ is shown as a solid line.

The height variation of Δp beneath the second lee-wave crest for FS, BL and BLI simulations is shown in Fig. 8(a) for a very small mountain of height 10 m. Data are shown for the idealized profile case with $U_t = 28$ m s^{-1} and $z_0 = 0.05$ m. To a very good approximation the BL results show that the pressure amplitude is constant through the boundary layer, whose depth is approximately 400 m. The low-level pressure amplitude in the free-slip case is larger and also exhibits significant changes with height, particularly above 100 m. As shown by Fig. 8(b), the same is true for a much higher mountain ($H = 300$ m) when the waves are sufficiently large to induce flow separation. Again Δp is independent of height through the boundary layer in the BL simulation, whereas the FS results contain more height variation and are of greater amplitude. The BLI results in Fig. 8(a) show that Δp is also independent of height when no turbulence parametrization is applied but the boundary-layer profile is retained, indicating that this height independence is caused by the changes in the basic-state profile rather than the direct effect of the turbulent dissipation on the wave motion itself. Note, however, that dissipation does account for the slight reduction in magnitude of Δp in the BL simulation relative to that in the BLI case. Also shown in Figs. 8(a) and (b) are the height variations of Δs in the BL simulations. Clearly the largest fractional deceleration occurs close to the ground and the magnitude of Δs decreases throughout the boundary layer.

The results presented in Fig. 8 also hint at an interesting and potentially powerful result. In the inviscid free-slip case the size of Δp, just above the top of the boundary layer, is comparable to the constant value observed in the BL case within the boundary layer. We shall return to this point in section 4 where we attempt to obtain linear lee-wave solutions for predicting the pressure amplitude within the boundary layer.
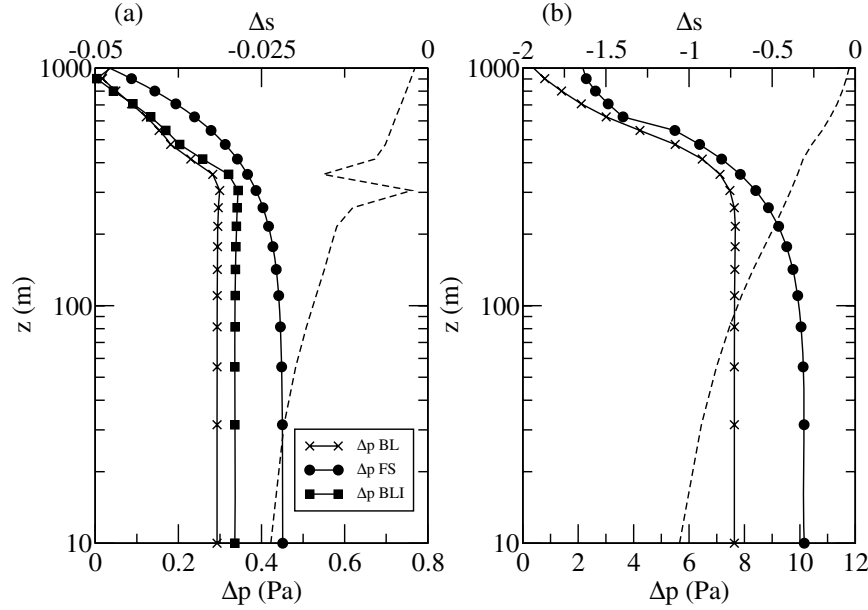
Figure 8. Near-surface vertical profiles of the pressure amplitude Δp (solid lines) and the fractional deceleration Δs (dashed), for the second downstream wavelength and mountain heights of (a) 10 m and (b) 300 m. Profiles of Δp are shown for BL, FS and BLI simulations with $U_t = 28$ m s^{-1}, $z_0 = 0.05$ m (see text). Note that profiles of Δs are presented for the BL simulations only and BLI simulations were not possible when $H = 300$ m.

4. LINEAR SOLUTIONS FOR THE NEAR-SURFACE FLOW

In this section we shall derive a set of equations for the turbulent motion beneath the wave crests and compare solutions for the fractional deceleration with the results from the numerical simulations. In reality the flow within a lee-wave rotor will clearly be highly nonlinear. In the interests of simplicity, however, and because we believe that linear dynamics will represent the main processes which lead to separation, we shall restrict attention to linear solutions. As demonstrated by Wood (1995), linear theory provides useful predictions of flow separation in turbulent flow over hills.

Two approaches to obtaining the linear solutions will be described. The first approach is numerical and solutions can be obtained to the full linear equations. The second involves further simplification to the equations which lead to an analytic solution. This expression is analogous to previously derived solutions for the acceleration of turbulent flow across a hill.

(a) A linear numerical solution for flow under the lee-wave crests

In what follows we shall assume that perturbations to the flow within the boundary layer are driven by an external pressure field due to the lee waves aloft. As shown previously (see Fig. 8) we expect this pressure perturbation to be independent of height throughout the depth of the boundary layer. Since above the boundary layer the Rossby number $R_o = \overline{U}/f\lambda \gg 1$, where f is the Coriolis force, we shall neglect the effects of rotation and assume the component of the flow parallel to the 2-D ridge axis is zero.

We define a 'wave-following' coordinate system whose surfaces follow the wave motion at the top of the boundary layer ($z = z_i$) and flatten off as the ground is

approached, namely

$$
\left.\begin{aligned}
X &= x, \\
\eta &= \frac{z z_i}{z_i + \delta},
\end{aligned}\right\} \tag{6}
$$

where δ is the vertical displacement of the streamlines about $z = z_i$ caused by the lee-wave motion. Applying Eq. (6) to the horizontal momentum and continuity equation and linearizing gives

$$
\overline{U} \frac{\partial u'}{\partial X} - \frac{\overline{U} z}{z_i} \frac{\partial \delta}{\partial X} \frac{\mathrm{d}\overline{U}}{\mathrm{d}\eta} + w' \frac{\mathrm{d}\overline{U}}{\mathrm{d}\eta} - \frac{\partial \tau'}{\partial \eta} = -\frac{\partial P'}{\partial X} \tag{7}
$$

and

$$
\frac{\partial u'}{\partial X} + \frac{\partial w'}{\partial \eta} = \frac{z}{z_i} \frac{\partial \delta}{\partial X} \frac{\mathrm{d}\overline{U}}{\mathrm{d}\eta}, \tag{8}
$$

where u' and w' are the horizontal and vertical components of the perturbation velocity field, respectively, τ' is the perturbation shear stress and $P' = p'/\rho_0$, where ρ_0 is a (constant) reference density. Note that the coordinate transformation allows us to evaluate the importance of the vertical transport of background shear by the wave motion. This is represented by the second term on the left-hand side of Eq. (7) and the right-hand side of Eq. (8). Assuming wave-like disturbances with wave number k, namely,

$$
(u', w', \delta, \tau', P') = \mathrm{Re}\{(\widehat{u}, \widehat{w}, \widehat{\delta}, \widehat{\tau}, \widehat{P}) \, e^{ikx}\} \tag{9}
$$

then gives

$$
ik\overline{U}\widehat{u} - ik\overline{U}\widehat{\delta} \frac{z}{z_i} \frac{\mathrm{d}\overline{U}}{\mathrm{d}\eta} - \frac{\partial \widehat{\tau}}{\partial \eta} = -ik\widehat{P} - \widehat{w} \frac{\mathrm{d}\overline{U}}{\mathrm{d}\eta} \tag{10}
$$

and

$$
\frac{\mathrm{d}\widehat{w}}{\mathrm{d}\eta} = -ik\widehat{u} + ik\widehat{\delta} \frac{z}{z_i} \frac{\mathrm{d}\overline{U}}{\mathrm{d}\eta}. \tag{11}
$$

For a specified pressure perturbation $\widehat{P}$, Eqs. (10) and (11) can be solved with suitable boundary conditions and an appropriate expression for $\widehat{\tau}$. For consistency with the turbulence closure used in the numerical simulations we specify an eddy viscosity closure of the form $\widehat{\tau} = 2\overline{K} \, \mathrm{d}\widehat{u}/\mathrm{d}z$, where $\overline{K} = l_m^2 \, \mathrm{d}\overline{U}/\mathrm{d}z$ is the basic-state eddy viscosity and l_m is the mixing length. Note that the factor of 2 comes from the contribution to $\widehat{\tau}$ from the perturbation eddy viscosity, which is equal to that from $\overline{K}$. Under neutral stratification l_m is specified by

$$
l_m^{-1} = l_0^{-1} + \{\kappa(z + z_0)\}^{-1}, \tag{12}
$$

where κ is the von Karman constant (assumed to be 0.4) and l_0 is a limiting scale for the mixing length (40 m). The imposed lower boundary condition is one of no-slip, whereas at the top of the boundary layer we assume that vertical wind shear and shear stress play no rôle in the dynamics. The balance in the horizontal momentum equation is therefore between horizontal advection and the wave-induced pressure gradient. The boundary conditions can be written as

$$
\widehat{u} = \widehat{w} = 0 \quad \text{at} \quad z = 0 \quad \text{and} \quad \widehat{u} = -\widehat{P}/\overline{U} \quad \text{at} \quad z = z_i. \tag{13}
$$

Equations (10) and (11) have been discretized on a staggered regular vertical mesh using second-order accurate centred finite differences. Solutions were obtained using

an iterative procedure whereby the discretized tridiagonal system for $\widehat{u}$ was first solved using LU-decomposition and lagged values of $\widehat{w}$ (initially zero). Equation (11) was then integrated upwards from the ground to obtain an updated profile of $\widehat{w}$. This procedure was repeated until convergence was obtained, typically after 10 to 20 iterations.

Note that one convenient approximation is to neglect the effects of the upstream wind shear, $\mathrm{d}\overline{U}/\mathrm{d}\eta$, in Eqs. (7) and (8). When such terms are neglected, solutions can be obtained without the need for iteration, since the vertical velocity does not enter into the horizontal momentum equation.

(b) A linear analytic solution by analogy with turbulent flow over a hill

If the shear terms are neglected and the basic-state velocity $\overline{U}(z)$ is replaced by a single velocity-scale, Eq. (7) then becomes the same equation for which solutions were initially sought in simple linearized theories for the inner region in turbulent flow over hills (e.g. Jackson and Hunt 1975; Mason and King 1985). Given the analogy between turbulent flow beneath lee waves and that over hills it is interesting to test linear predictions for the latter against the results from the numerical simulations. Note that, for the case of flow over a hill, the importance of vertical wind shear was recognized in later theories (e.g. Hunt *et al.* 1988; Belcher 1990). However, since the vertical velocity which advects the basic-state shear is clearly very different to that associated with lee waves we shall restrict attention to the earlier solutions in which the shear was neglected. Although admittedly Mason and King (1985) have heuristically improved the accuracy of the original Jackson and Hunt (1975) solution, their expression for the fractional acceleration does not converge as the surface is approached. Since in order to predict flow separation such convergence is essential, we shall restrict attention here to the original Jackson and Hunt solution. For flow over a 2-D sinusoidal ridge with wave number k this can be be written as

$$u'/\overline{U} = \frac{\Delta p_{\mathrm{hill}}}{\overline{U}(l)\overline{U}(z)} \,\mathrm{Re}\left\{ 1 - \frac{K_0(2\sqrt{\mathrm{i}kz\overline{U}(l)/2\kappa u_*})}{K_0(2\sqrt{\mathrm{i}kz_0\overline{U}(l)/2\kappa u_*})}\, \mathrm{e}^{\mathrm{i}kx} \right\}, \qquad (14)$$

where K_0 is the zeroth-order modified Bessel function, l is the inner-region depth and Δp_{hill} is the amplitude of the pressure perturbation due to the hill. The latter is determined by inviscid dynamics in the outer region of the flow. The depth-scale for the inner region, l, is determined by balance between the perturbation stresses and the perturbation pressure gradient. For flow over a sinusoidal ridge, l takes the implicit form

$$\frac{lk}{\pi} \log\left(\frac{l}{z_0}\right) = \kappa^2, \qquad (15)$$

where, following Wood (1992), the hill length-scale L which appeared in Jackson and Hunt's original expression has been replaced by one quarter of the sinusoidal hill wavelength, or equivalently $\pi/2k$. The importance of defining l lies in the evaluation of the single velocity-scale $\overline{U}(l)$ in Eq. (14). For flow over a hill, the pressure perturbation Δp_{hill} is assumed to be related to the hill slope θ, and a further velocity-scale $\overline{U}(h_{\mathrm{m}})$ in the outer region of the flow by $\Delta p_{\mathrm{hill}} = \theta\overline{U}(h_{\mathrm{m}})^2$ (e.g. Hunt *et al.* 1988). When concerned with the flow under a lee-wave wavelength, however, it is appropriate to replace Δp_{hill} by the lee-wave pressure perturbation Δp. Similarly, when calculating the inner-region depth l we shall replace k by the lee-wave horizontal wave number in Eq. (15).

Note that the above linear theories are typically applied to hills with horizontal length-scales of O(1 km), whereas the lee-wave wavelengths are usually an order of magnitude longer. One consequence of this is that the values of l in the lee-wave context are significantly greater than those usually quoted for flows over hills. For example, for a hill with a wavelength of 1 km, $l \sim 14$ m when $z_0 = 0.05$ m. In contrast, for a lee-wave wavelength of 10 km, l is approximately 105 m and for a 20 km wavelength l increases to 194 m, a significant fraction of the boundary-layer depth. We should also note that, strictly speaking, Eq. (15) relies on the fact that the boundary-layer has a logarithmic wind profile. Clearly for the larger values of l in the lee-wave context this may be a poor approximation. There is, therefore, some uncertainty attached to the value of $\overline{U}(l)$ in Eq. (14).

(c)   *Comparisons between linear solutions and numerical simulations*

Vertical profiles of Δs under the lee-wave crests are presented in Fig. 9 for the idealized $U_t = 28$ m s^{-1} BL case with a roughness length of 0.05 m. The Jackson and Hunt (Eq. (14)) and the numerical linear solutions, both with and without the vertical shear terms, are presented. These solutions were based on lee-wave horizontal wave numbers and surface values of Δp deduced from the simulations. Again the latter was measured across the second wavelength downwind of the mountain. Note that, to account for alterations to the mean flow due to turbulent or wave drag, the basic-state winds used in the calculations were the wavelength-averaged profiles, $U_\lambda(z)$. Results are shown for mountain heights of 10 and 300 m and for comparison purposes the Δs values in the corresponding BLASIUS simulations are also shown. In a qualitative sense it appears that all the linear solutions reproduce the behaviour observed in the simulations. The closest agreement with the simulations comes from the full linear numerical solution in which the vertical shear terms are retained. In the $H = 10$ m case these linear predictions are very close to those obtained in the BLASIUS simulation. At $H = 300$ m the magnitude of Δs is under-predicted by approximately 9%. For both mountain heights the linear numerical prediction of Δs is somewhat reduced in magnitude when the vertical shear terms are neglected, implying that vertical advection of the basic-state wind shear plays a rôle in enhancing the deceleration under the wave crests. For the $H = 300$ m case the contribution to $|\Delta s|$ from this vertical advection is approximately 15%. The Jackson and Hunt solution appears to significantly underestimate the magnitude of Δs in both the small and large mountain cases. Whilst this can be partly attributed to the neglect of vertical shear, Fig. 9 suggests this alone will only result in a slight under-prediction. Furthermore, tests performed with the numerical solution (with no shear) to Eq. (7) in which $\overline{U}(z)$ was replaced by $\overline{U}(l)$ gave very similar results to those provided by Eq. (14). Thus it seems that this underestimate is largely a result of the selection of a single velocity-scale $\overline{U}(l)$ in the inner region. This could possibly be corrected via an ad hoc (and probably case-dependent) reduction in the inner-region depth. Given the uncertainties regarding the scaling for l in the (long wavelength) lee-wave case this might be not be completely without justification. However, this clearly requires some further investigation.

Figure 9 highlights the rôle of the turbulent stresses in determining the flow perturbations within the boundary layer. If the dynamics were truly inviscid we might expect $-\overline{U}\widehat{u} \sim \widehat{P}$ and, since the pressure gradient is independent of height, $|\Delta s| \propto 1/\overline{U}^2$. The decrease of the boundary-layer winds near the surface would then imply a $|\Delta s|$ profile whose vertical gradient increased as the ground was approached. Figure 9 shows that this is clearly not the case. Instead the gradient of $|\Delta s|$ decreases close to
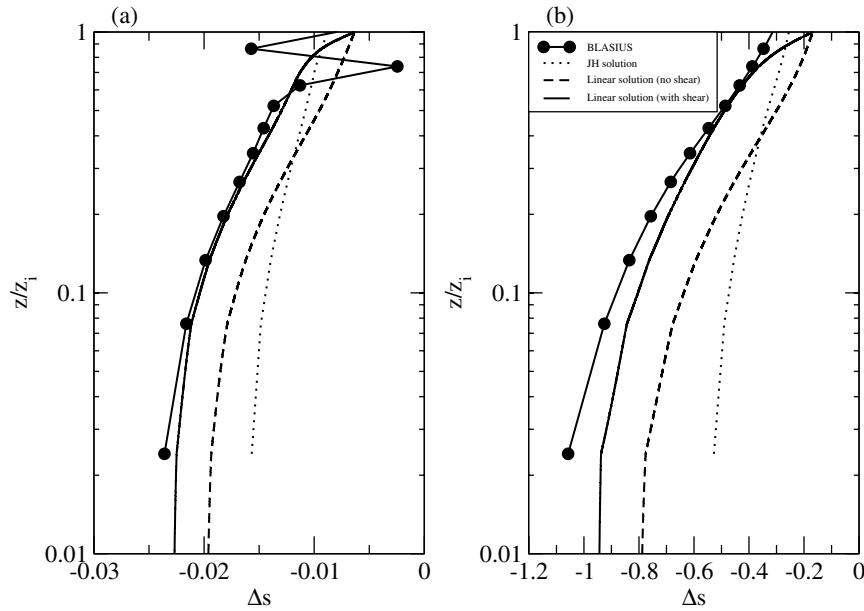
Figure 9. Vertical profiles of the minimum fractional deceleration Δs under lee waves in a BL flow with $U_t = 28$ m s^{-1}, $z_0 = 0.05$ m (see text) for mountain heights of (a) 10 m and (b) 300 m. The quantities shown are results from the numerical simulations beneath the second wave crest (solid line and circles), the linear Jackson–Hunt solution (dotted) and the linear numerical solutions with (solid line) and without (dashed) the shear terms. The linear solutions shown were obtained using the pressure amplitude Δp diagnosed at the surface in the corresponding numerical simulations.

the ground and, as shown by the numerical linear solutions, very close to the surface Δs is in fact almost independent of height. This result is consistent with that seen in the flow over hills case, where the fractional speed-up over the hill crest is independent of height in the lower portion of the inner region (e.g. Newley 1985). Clearly the turbulent stresses have a significant impact on the size of the flow perturbations close the ground and the flow is not controlled by simple inviscid dynamics.

For a range of mountain heights Fig. 10 shows how the linear prediction of Δs at the surface corresponds to the results from series of $U_t = 28$ and 36 m s^{-1} BL simulations, with roughness lengths of 0.05 and 0.005 m. Again these linear solutions have been obtained using values of Δp and k deduced from the simulations. Also shown are results from simulations based on the two radiosonde profiles with $z_0 = 0.05$ m. Since the linear numerical solution in which the shear terms are retained clearly provides the most accurate estimates of Δs, only these solutions are presented. Figure 10 demonstrates that in all cases the linear estimate performs reasonably well right up to the point where the waves are sufficiently large that flow separation occurs. For the small amplitude waves, where $|\Delta s|$ is significantly less than unity, the linear solutions agree very closely with the results of the simulations for all cases. As separation is approached ($\Delta s \rightarrow -1$) and the flow becomes increasingly nonlinear, the linear estimates have a tendency to slightly under-predict the deceleration in the majority of cases. Beyond separation the linear solutions then begin to over-predict the magnitude of Δs. Given the nonlinear nature of the near-surface flow as separation is approached, the overall reliability of the linear solution is perhaps somewhat surprising. We should note, however, that some degree of nonlinearity is already incorporated into the linear estimate since the solution is forced
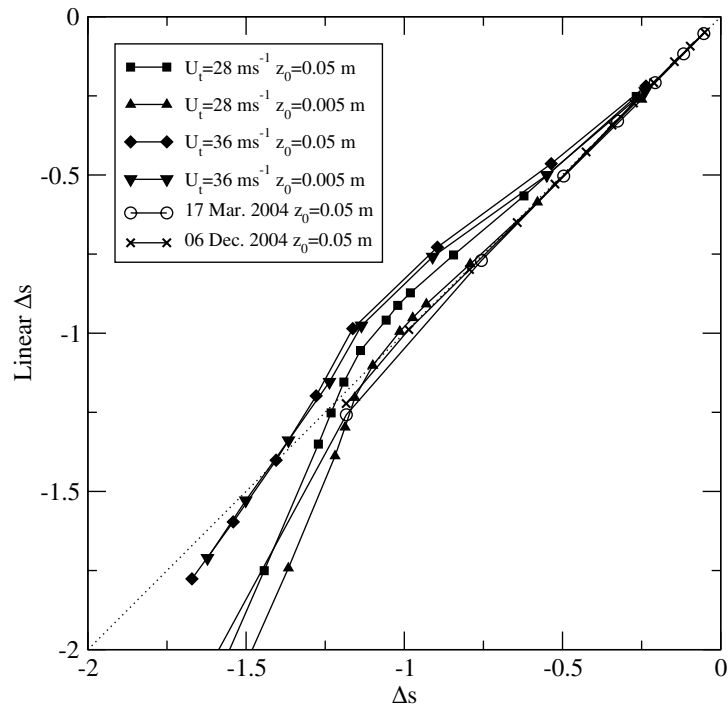
Figure 10. A comparison of the linear theory solution for Δs at the surface with the values diagnosed from the numerical simulations at the lowest grid level under the second lee-wave crest. Results are shown for a range of mountain heights for the $U_t = 28$ and 36 m s^{-1} BL cases with $z_0 = 0.05$ and 0.005 m (see text). Also shown are the results for the two cases where the basic-state profiles were obtained from radiosonde profiles (17 March and 6 December 2004). The linear results shown are from the numerical solutions in which the shear terms are retained.

by the pressure amplitude diagnosed from the numerical simulations. In order to form a more complete linear theory we clearly require an independent estimate of this pressure amplitude. This is pursued in section 4(d).

The linear solutions for Δs can be used to estimate the critical wave amplitude required for rotor formation. The solid curve presented in Fig. 7 shows the linear prediction of the critical normalized pressure amplitude, $\Delta p / u_*^2$, as a function of λ / z_0. The curve shown was computed using the most accurate numerical solution (in which the shear terms are retained) and has been found to be valid for different combinations of wavelengths, roughness lengths and friction velocities. The critical amplitudes were obtained by simply computing the surface values of Δs for a given (arbitrary) imposed pressure and then extrapolating the results to obtain the values of Δp at which $\Delta s = -1$. Note that, for the purposes of producing the curve shown, the basic-state wind profiles within the boundary-layer were assumed to have a logarithmic form. However, the results were not sensitive to this choice. Tests performed using the actual 1-D BL profiles from the idealized or radiosonde simulations produced curves which were very similar to that shown in Fig. 7. This lack of sensitivity suggests that for the numerical simulation results depicted in Fig. 7, the differences in the way the critical values of $\Delta p / u_*^2$ depend on λ / z_0 for idealized and radiosonde profiles are not caused by differences in the structure of the boundary layer. Given that when the waves are of small amplitude the linear solutions for Δs compare closely with the results from all

types of numerical simulation (see Fig. 10), it is likely the differences in behaviour are caused by nonlinearity as the waves become large enough that separation occurs.

The linear critical pressure amplitude shown in Fig. 7 behaves in a similar manner to that deduced from the numerical simulations; both show a tendency to increase with increasing λ/z_0. It is worth noting here that, up to this point, the expectation that the critical value of $\Delta p/u_*^2$ should be a function of λ/z_0 was largely an empirical result. The collapse of the linear predictions for different combinations of λ and z_0 give this result further credibility. Clearly, however, the linear prediction for the critical amplitude is an overestimate compared to the results from the simulations. This is consistent with the fact that as separation is approached the linear solution generally under-predicts the magnitude of Δs (see Fig. 10). Note though that, because (out of necessity) the linear prediction of the critical wave amplitude is based on upwind rather than wavelength averaged wind profiles, no account is taken of nonlinear modification to the mean flow. The agreement between the linear solutions and the numerical simulations implied by Fig. 7 is therefore not as close as that shown in Fig. 10.

(d) An estimate for the lee-wave pressure perturbation

In terms of developing a practical tool for rotor prediction it is clearly necessary to predict the lee-wave amplitude as well as the response of the near-surface flow. In this section we shall attempt to obtain linear estimates of the wave-induced pressure perturbation which could then be used to force the solutions described in section 4. It is worth bearing in mind, however, that under certain conditions the lee-wave field can be highly nonlinear, even when generated by mountains with low slope and when $NH/\overline{U} \ll 1$ (e.g. Smith 1976; Durran and Klemp 1982). For example, when the waves are generated by mountains which are significantly broader than the lee-wave wavelength or when the upstream profiles contain sharp stable layers, the amplitude will be determined by nonlinear processes. Nevertheless, linear models have proved generally useful for predicting observed lee-wave motion over complex, but moderate, terrain (e.g. Vosper and Mobbs 1996; Shutts 1997; Vosper 2003).

Following Sawyer (1960) the linear solution for a trapped lee wave with positive horizontal wave number k_r can be written as $w'(x, z) = \text{Re}\{\widehat{w}\, e^{ik_r x}\}$, where

$$\widehat{w} = -2\overline{U}(z=0) \left\{ \frac{f(z)}{f'(z=0)} k_r \widehat{h}(k_r) \right\} \tag{16}$$

and Eq. (16) is valid downstream of the mountain only. In the above f is a function which satisfies Eq. (3) such that, at the resonant wave number k_r, $f = 0$ at $z = 0$. The quantity f' is $\partial f/\partial k$, $\widehat{h}$ is the Fourier transform of the mountain and the factor 2 arises from a contribution from a negative wave number $(-k_r)$, which itself is an artifact of defining $\widehat{h}$ to be an integral over positive and negative wave numbers. Equation (3) can be discretized using centred finite differences and resonant solutions (which satisfy $f(0) = 0$) can then be sought for any given ℓ^2 profile. The appropriate upper boundary condition is one which ensures either upward group velocity or exponential decay of the waves, depending on the sign of $\ell^2 - k^2$ at the upper boundary. The solution of Eq. (3) is an eigenvalue problem which yields a value for the complex resonant wave number k_r, the imaginary part of which gives an indication of the degree of wave trapping since its reciprocal is a horizontal decay scale. Further details of the technique used to obtain solutions are given by Shutts et al. (1994) and Vosper and Mobbs (1996). Linear solutions for the pressure amplitude $\widehat{p}$ can be obtained by substitution of $\widehat{w}$ and $\widehat{u}$ into

the Fourier transformed horizontal momentum equation, where $\widehat{u}$ is the corresponding horizontal velocity amplitude, itself obtained from the continuity equation.

Figure 11 shows a comparison between the pressure amplitude profiles obtained from the above linear solution and Δp, measured in a $U_t = 28$ m s^{-1} FS idealized simulation. The results shown are for a very small mountain ($H = 10$ m) and Δp was determined from the second wavelength. The linear solution for the inviscid free-slip (FS) profile compares reasonably well with the FS numerical results with a slight tendency for the linear solution to under-predict the numerical result near the ground. The linear resonant wavelength was 11.8 km, which is very close to that determined from the simulation. Linear solutions have also been obtained when the profile contains a boundary layer. Note, however, that such solutions are somewhat ill defined since the amplitude of the waves depends to an extent on the velocity $\overline{U}$ at $z = 0$ (see Eq. (16)). In the no-slip case this is clearly zero, implying no wave generation. In an attempt to avoid this problem solutions for the BL profiles were calculated by simply replacing $\overline{U}(0)$ in Eq. (16) by the wind at the lowest model grid level (10 m). As shown by Fig. 11, the solution obtained in this way compares closely with the inviscid (BLI) numerical results in which the boundary-layer modifications to the profile are retained. The amplitude of the linear solution is, however, highly sensitive to the choice of height of the lower boundary. Although the shape of the profile is retained, increasing this height above 10 m reveals that, as one might expect, the amplitude is proportional to the wind speed at the lower boundary. Consequently, increasing the lower boundary height from 10 to 50 m produces an increase in amplitude of roughly 30%. When the lower boundary height is reduced from 10 to 1 m (using 1-D BL solutions with a lowest grid level at 0.25 m) the amplitude fluctuates rapidly and changes by as much as 15% over this range. This latter behaviour is presumably connected with the fact that ℓ^2 becomes unbounded as the ground is approached. Despite the seemingly fortuitous level of agreement shown in Fig. 11, it is clear that inviscid linear calculations such as these will in general not provide a reliable estimate of the lee-wave pressure amplitude within the boundary layer.

As discussed in section 3, comparisons of the pressure amplitude in the no-slip and free-slip simulations show that the constant value of Δp observed within the boundary layer is comparable to the value in the FS case, at some height above the boundary-layer top ($z = z_i$). This result, if generally true, would imply that a linear estimate for the lee-wave pressure could be obtained by simply obtaining solutions for profiles without any boundary-layer modification. The extent to which this is true in general is demonstrated by Fig. 12(a), in which linear pressure predictions obtained using FS profiles are plotted against Δp measured across the second wavelength in BL simulations. Data are presented for the idealized ($U_t = 28$ and 36 m s^{-1}) and radiosonde profile simulations, each with three values of z_0 (0.005, 0.01 and 0.05 m). The mountain height is 100 m. In all cases the linear estimates for Δp shown in Fig. 12(a) are taken at a height $z = 1.4z_i$, where z_i is defined to be the height above which the basic-state shear stress has decayed to below 10% of its surface value. This particular height was chosen since this is roughly the height at which the FS pressure amplitude is equal to the near-surface value in the BL simulations based on the idealized profiles (see Fig. 8, for example). Figure 12(a) shows that the linear estimate of Δp at $z = 1.4z_i$ is a reasonable one for all the cases considered apart from the simulations based on the 6 December radiosonde profile. In the latter case, the inviscid linear solution over-predicts Δp in the boundary layer. The reasons for this are not clear (though note they could be compensated for by taking the linear pressure from a somewhat higher level, $z \sim 2z_i$) but given the slightly different behaviour of the near-surface flow noted in Fig. 7 for the radiosonde profile simulations, it seems likely that the flow in this case is more nonlinear. It is of course also possible
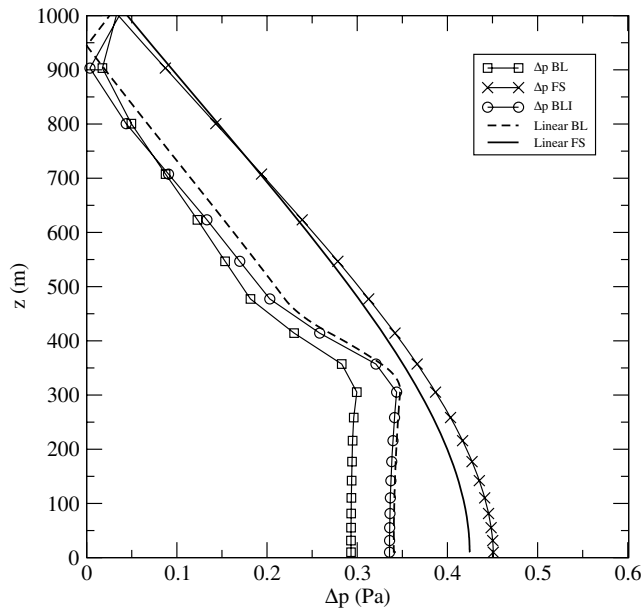
Figure 11. The height variation of the linear pressure amplitude derived from solutions to Eq. (3) for the $U_t = 28$ m s^{-1} idealized profile with a 10 m high mountain. Quantities shown are solutions for the inviscid free-slip FS profile (solid line) and the BL profile (dashed) with roughness length 0.05 m. Also shown are profiles of Δp across the second wavelength determined from corresponding numerical simulations. The FS, BL and BLI results are denoted by crosses, squares and circles, respectively.

that the correct choice of height will vary from case to case, depending on the details of the structure of the boundary layer.

The extent to which the linear estimate for the pressure amplitude is useful for waves with larger amplitude than those examined in Fig. 12(a) is demonstrated by Fig. 12(b), which shows the variation of Δp with mountain height for the BL simulations with $U_t = 28$ and $z_0 = 0.05$ m. It appears that the linear predictions at $z = 1.4 z_i$ are reasonable for mountain heights as high as around 250 m. Since this is close to the point at which rotors first appear (at $H = 290$ m), it would seem that in this case at least, in combination with the linear solutions of section 4(a) or the results presented in Fig. 7, linear theory could be used to give a reliable prediction of rotor formation.

5. CONCLUSIONS

This study has demonstrated how the process of flow deceleration, which leads to separation and the formation of rotors beneath lee-wave crests, depends primarily on the amplitude of the lee-wave pressure field, and to a somewhat lesser extent, the surface roughness and lee-wave wavelength. There is a clear analogy between the mechanism by which lee waves decelerate the near-surface flow, eventually leading to separation, and the process of acceleration of turbulent flow across a hill. In both situations the near-surface flow is primarily controlled by an external (height-independent) pressure field, which is relatively unaffected by turbulent dissipation within the boundary layer. Further, in both cases the vertical advection of the mean wind shear plays a minor rôle in contributing to the acceleration and deceleration.
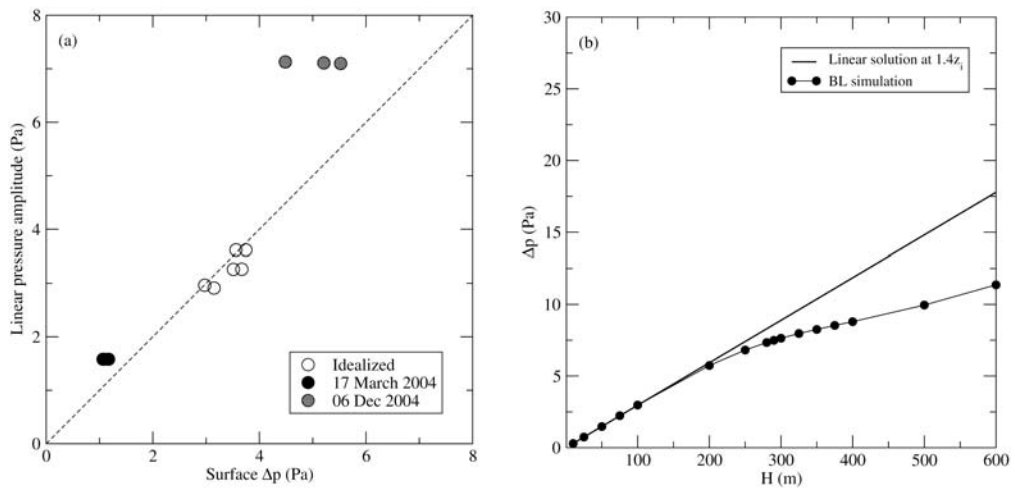
Figure 12.   (a) The linear prediction for the pressure amplitude at a height $1.4z_i$ plotted against Δp across the second wavelength diagnosed from the BL numerical simulations. The linear predictions are based on solutions to Eq. (3) with no boundary-layer modification to the basic-state profile. The mountain height is fixed at 100 m. Data are shown for idealized profile simulations with $U_t = 28$ and 36 m s^{-1} (open circles) and for the simulations using the two radiosonde profiles (solid and shaded circles). In each case results are presented for three values of z_0 (0.005, 0.01 and 0.05 m). (b) The dependence of the pressure amplitude on H for the idealized $U_t = 28$ m s^{-1} profile when $z_0 = 0.05$ m. The quantities shown are linear predictions (as in (a)) at $z = 1.4z_i$ and Δp at the surface determined from the BL simulations across the second wavelength. See text for explanation of symbols.

The results presented here have shown how, to a good approximation, the near-surface deceleration under the wave crests responds in a linear manner to the lee-wave pressure field. This is true almost right up to the point where reversal occurs. As expected, beyond this point, when a rotor forms under a wave crest, the flow behaviour is more nonlinear. Nevertheless, from the point of view of predicting the occurrence of rotors the simple linear numerical solutions (or alternatively the Jackson and Hunt solution with perhaps some adjustment to the inner-region velocity-scale) describe the flow adequately well. When coupled with a prediction of the pressure field, a practical tool for rotor forecasting could be developed. As suggested here, this prediction could involve solutions to Eq. (3) obtained using either full profiles, which include the boundary layer (though noting the likely sensitivity of the solutions to the choice of grid), or by calculating the pressure at some height above z_i using modified profiles in which the boundary layer was somehow removed. Clearly the latter would involve some arbitrary assumptions about the form of the profile before any modification by the boundary-layer.

It is worth mentioning here that in the context of flow over hills a known defect of mixing-length turbulence closure models is a tendency to over-predict (compared with second-order closure models) the effect of the perturbation turbulent stresses near the top of the inner region (Newley 1985; Belcher 1990; Wood 1995). This results in spuriously enhanced mixing, thus reducing the impact of the mean velocity shear on the velocity perturbations. In general, compared with second-order closure models, mixing-length closure models of flows over hills tend to over-predict the magnitude of Δs very close to the ground, whilst under-predicting the values near the top of the inner region. It seems likely that similar effects may occur in the context of lee-wave rotors, and since

the predictions of Δs and flow separation presented here were obtained using a first-order closure scheme, compared with reality the critical wave amplitudes required for rotor formation might actually be a slight overestimate.

The above effect, whilst possibly important, is likely to be small compared to changes in the flow behaviour caused by the introduction of three-dimensionality. The possibility of the low-level flow diverting around regions of adverse pressure gradient rather than separating from the surface implies that the critical wave amplitudes required for rotor formation are likely to be larger than those for 2-D wave fields. Further, the complex structure and unsteadiness that occur in separated 3-D flows past hills indicates that the process of separation and rotor formation might be far more complicated than that considered here. Clearly much further work is required in this area.

REFERENCES

Baines, P. G.	1995	*Topographic effects in stratified flow*. Cambridge University Press
Belcher, S. E.	1990	'Turbulent boundary-layer flow over undulating surfaces'. PhD thesis, University of Cambridge
Doyle, J. D. and Durran, D. R.	2002	The dynamics of mountain-wave-induced rotors. *J. Atmos. Sci.*, **59**, 186–201
Durran, D. R. and Klemp, J. B.	1982	The effects of moisture on trapped mountain lee waves. *J. Atmos. Sci.*, **39**, 2490–2506
	1983	A compressible model for the simulation of moist mountain waves. *Mon. Weather Rev.*, **111**, 2341–2361
Gal-Chen, T. and Somerville R.	1975	On the use of a coordinate transformation for the solution of the Navier–Stokes equations. *J. Comp. Phys.*, **17**, 209–228
Hertenstein, R. F. and Kuettner, J. P.	2005	Rotor types associated with steep lee topography: influence of the wind profile. *Tellus A*, **57**, 117–135
Holmboe, J. and Klieforth, H.	1957	Investigation of mountain lee waves and the air flow over the Sierra Nevada. Final Report. Contract No. AF19(604)-728, University of California ADNo. 133606, Dept. of Meteorology, University of California, Los Angeles, USA
Hunt, J. C. R., Leibovich, S. and Richards, K. J.	1988	Turbulent shear flows over low hills. *Q. J. R. Meteorol. Soc.*, **114**, 1435–1470
Jackson, P. S. and Hunt, J. C. R.	1975	Turbulent wind flow over a low hill. *Q. J. R. Meteorol. Soc.*, **101**, 929–956
Jiang, Q. F., Doyle, J. D. and Smith, R. B.	2006	Interaction between trapped waves and boundary layers. *J. Atmos Sci.*, **63**, 617–633
Kuettner, J.	1939	Zur entstehung der föhnwalle. *Beitr. Phys. Frei Atmos.*, **25**, 251–299
Leonard, B. P., MacVean, M. K. and Lock, A. P.	1993	Positivity-preserving numerical schemes for multidimensional advection. NASA Technical Memo. 106055, ICOMP-93-05
Lyra, G.	1943	Theorie der stationären Leewellenstromung in freier Atmosphäre. *Z. Angew. Math. Mech.*, **23**, 1–128
Mason, P. J. and King, J. C.	1985	Measurements and predictions of flow and turbulence over an isolated hill of moderate slope. *Q. J. R. Meteorol. Soc.*, **111**, 617–640
Mobbs S. D., Vosper, S. B., Sheridan, P. F., Cardoso, R., Burton, R. R., Arnold, S. J., Hill, M. K., Horlacher, V. and Gadian, A. M.	2005	Observations of downslope winds and rotors in the Falkland Islands. *Q. J. R. Meteorol. Soc.*, **131**, 329–351

Nance, L. B.	1997	On the inclusion of compressibility effects in the Scorer parameter. *J. Atmos. Sci.*, **15,** 362–367
Newley, T. M. J.	1985	'Turbulent air flow over hills'. PhD thesis, University of Cambridge
Piacsek, S. A. and Williams, G. P	1970	Conservation properties of convection difference schemes. *J. Comput. Phys.*, **6,** 392–405
Ralph F. M., Neiman, P. J., Keller, T. L., Levinson, D. and Fedor, L.	1997	Observations, simulations and analysis of nonstationary trapped lee waves. *J. Atmos. Sci.*, **54,** 1308–1333
Ross, A. N. and Vosper, S. B.	2003	Numerical simulations of stably stratified flow through a mountain pass. *Q. J. R. Meteorol. Soc.*, **129,** 97–115
Sawyer, J. S.	1960	Numerical calculation of the displacements of a stratified airstream crossing a ridge of small height. *Q. J. R. Meteorol. Soc.*, **86,** 326–345
Scorer, R. S.	1949	Theory of lee waves of mountains. *Q. J. R. Meteorol. Soc.*, **75,** 41–56
Shutts, G. J.	1997	Operational lee wave forecasting: Directional wind shear. *Meteorol. Appl.*, **4,** 23–35
Shutts, G. J., Healey, P. and Mobbs, S. D.	1994	A multiple sounding technique for the study of gravity waves. *Q. J. R. Meteorol. Soc.*, **120,** 59–77
Smith, R. B.	1976	The generation of lee waves by the Blue Ridge. *J. Atmos. Sci.*, **33,** 507–519
Smith, R. B., Jiang, Q. F. and Doyle, J. D.	2006	A theory of gravity wave absorption by a boundary layer. *J. Atmos. Sci.*, **63,** 774–781
Vosper, S. B.	2003	Development and testing of a high resolution mountain-wave forecasting system. *Meteorol. Appl.*, **10,** 75–86
	2004	Inversion effects on mountain lee waves. *Q. J. R. Meteorol. Soc.*, **130,** 1723–1748
Vosper, S. B. and Mobbs, S. D.	1996	Lee waves over the English Lake District. *Q. J. R. Meteorol. Soc.*, **122,** 1283–1305
Wood, N.	1992	'Turbulent flow over three-dimensional hills'. PhD thesis, University of Reading
	1995	The onset of separation in neutral, turbulent flow over hills. *Boundary-Layer Meteorol.*, **76,** 137–164
Wood, N. and Mason, P. J.	1993	The pressure force induced by neutral, turbulent flow over hills. *Q. J. R. Meteorol. Soc.*, **119,** 1233–1267